The DOI for this manuscript is doi:
10.1175/2009JTECHA1260.1

Vorticity from line-of-sight lidar velocity scans

Martin Weissmann[1], Andreas Dörnbrack[1] and James D. Doyle[2]

[1]*Deutsches Zentrum für Luft- und Raumfahrt, Institut für Physik der Atmosphäre, Oberpfaffenhofen, Germany*

[2]*Naval Research Laboratory, Monterey, California, USA*

Draft note for submission to Journal of Atmospheric and Oceanic Technology

T-REX special issue

revised version

21 July 2009

Corresponding author address:
Dr. Martin Weissmann,
DLR Oberpfaffenhofen
D-82230 Wessling, Germany
E-Mail: Martin.Weissmann@DLR.DE

Abstract

A method is presented to compute the spanwise vorticity in polar coordinates from 2D vertical cross-sections of high-resolution line-of-sight Doppler wind lidar observations. The method uses the continuity equation to derive the velocity component perpendicular to the observed line-of-sight velocity, which then yields the spanwise vorticity component. The results of the method are tested using a ground-based Doppler lidar, which was deployed during the Terrain-induced Rotor Experiment (T-REX). The resulting fields can be used to identify and quantify the strength and size of vortices, such as those associated with atmospheric rotors. Furthermore, they may serve to investigate the dynamics and evolution of vortices and to evaluate numerical simulations. A demonstration of the method and comparison with high resolution numerical simulations reveals that the derived vorticity can explain 66% of the mean square vorticity fluctuations, has a reasonably skillful magnitude and exhibits no significant bias, and is in qualitative agreement with model-derived vorticity.

1. Introduction

The T-REX field campaign was carried out in spring 2006 in the Owens Valley, California, USA (Grubišić et al. 2008). The main focus of the experiment was the investigation of the coupled mountain wave rotor system in the lee of the Sierra Nevada. One of the primary objectives is to study the internal dynamics of rotors and their interaction with boundary-layer processes near the earth's surface.

Atmospheric rotors are characterized by strong downslope surface winds in the lee of a mountain range that decelerate rapidly to a weaker, transient and turbulent flow, often directed back toward the mountain (e.g., Holmboe and Klieforth 1957; Kuettner 1959; Doyle and Durran 2002, Doyle et al. 2009). Based on 3D high-resolution numerical simulations, Doyle and Durran (2007) proposed that the largest hazard for aviation is actually not the whole rotor, but smaller vortices, which they called subrotors. These vortices can be produced along a shear line that is generated by boundary layer separation due to strong downslope winds and lifted aloft by the lee wave circulation (Doyle et al. 2009). One of the major challenges for T-REX is to observe these subrotor vortices, to estimate the strength of the horizontal vorticity, and to investigate their characteristics.

In this study, high-resolution scanning Doppler lidar observations taken during T-REX are analyzed and a method for deriving tangential velocity (V_ϕ) and vorticity fields from lidar line-of-sight velocities (V_r) is presented (see Fig. 1 for the definition of the coordinate system). During T-REX rotor events, most lidar observations were made in a vertical cross-section mode along a baseline 260° from north to 80° from north, which is roughly parallel to the main flow and perpendicular to the valley axis and the Sierra Nevada Ridge. The observations were made by the Institut für Physik der Atmosphäre of the Deutsches Zentrum für Luft- und Raumfahrt (DLR) using a scanning 2 μm coherent Doppler lidar system from Lockheed Martin Coherent

Technologies (WindTracer®, for details see w*ww.lockheedmartin.com/ssc/coherent/products/windtracer/Specifications.html*). The lidar was situated on the alluvial slope of the Owens Valley at latitude = 36.79°N, longitude = 118.21°W, and 1240 m MSL, which is approximately 2 km west of the town of Independence. The valley is confined by the Sierra Nevada to the west, which includes several peaks above 4000 m MSL and the highest peak in the lower United States, and the Inyo Mountains to the east with peaks exceeding 3000 m MSL. The width of the valley is approximately 20-25 km. The time required for a full lidar cross-section was between 30 and 150 s during the T-REX field campaign depending on scanning speed. The cross sections used in this note were taken over a time period of 90 s. The resolution of this cross section is 105 m along the lidar beam and 2° elevation.

Doppler lidars only measure the wind component V_r in the direction of the lidar beam, whereas either u and v or V_r and V_ϕ are needed to derive spanwise vorticity fields. Under relatively stationary flow conditions, this can be solved by observations with two (or more) ground-based lidar systems or by making observations from several directions with a lidar mounted on a moving platform, e.g. an aircraft (Reitebuch et al. 2003). Atmospheric rotors during T-REX, however, were highly transient and associated with strong turbulence.

In addition to the DLR lidar, the Arizona State University (ASU) operated a similar Doppler lidar during the T-REX field campaign. Both lidars performed co-planar lidar observations with the goal of deriving the horizontal and vertical velocity through a combination of both data sets through dual Doppler analysis (Drechsel et al. 2008, Hill et al. 2008). Results from dual Doppler can also be used to derive spanwise vorticity, but the combination of two different data sets inevitably leads to errors due to the time difference of the observations (up to about 30-150 s with the scan strategy during T-REX). Furthermore, the volume of the observations is never completely the same due to the observation geometry. Thus, it is concluded

that in events with strong turbulence and transient flow, the time sequencing and differences of the observational volume likely lead to significantly larger errors than the method presented in this note. For example, relatively small vortices propagate with the mean flow, which can lead to a displacement of up to 600 m (nearly 6 range gates) in 30 s for a wind speed of 20 m s^{-1}.

This note presents an alternative method that exploits the continuity equation to derive V_ϕ and the spanwise vorticity from vertical slice line-of-sight observations of a single lidar (Section 2). This approach has the advantage that the time difference between two adjacent observations is in the range of only 0.2 to 1 s. The errors of lidar V_r observations are small compared to the velocity fluctuations associated with turbulent flows as e.g. in rotors. Errors of coherent 2 μm Doppler lidars are often estimated to be on the order of 0.1 m s^{-1} under favorable conditions and may increase by a factor of approximately 2-3 at a lower signal-to-noise ratio (Grund et al. 2001, Chai et al 2004).

The main errors for the derived V_ϕ and vorticity fields are expected to occur due to flow divergence perpendicular to the plane of the lidar cross-section. For this reason, the errors of the calculation due to divergent lateral flow are investigated with tests using 2D and 3D high resolution numerical simulations with the atmospheric portion of the Coupled Ocean/Atmosphere Mesoscale Prediction System (COAMPS®) in Section 3. Furthermore, the application of the calculation to T-REX observations is also shown in Section 3. The discussion of the results is presented in Section 4.

2. Tangential velocity and vorticity calculations derived from V_r observations

The tangential velocity V_ϕ (i.e. velocity component perpendicular to V_r) can be calculated for the grid points in each quadrant through the use of the 2D continuity equation in polar coordinates and the application of a boundary condition such that the vertical velocity is zero at

the surface. It could also be calculated for the whole hemicycle starting at $\phi = 0°$, but errors of the calculation accumulate with every elevation increment. It follows that it is more accurate to begin the calculation from both sides (i.e. at $\phi = 0°$ and $\phi = 180°$, respectively).

Assuming that there is no divergence perpendicular to the plane of the lidar observations ($r\phi$-plane), the continuity equation in polar coordinates (r, ϕ) is

$$\frac{1}{r}\frac{\partial}{\partial r}\left(rV_r\right)+\frac{1}{r}\frac{\partial V_\Phi}{\partial \Phi}=0 \quad , \tag{1}$$

where r is the radial distance from the lidar, ϕ is the elevation angle and V_r and V_ϕ are the radial and tangential velocities respectively. $\partial V_r/\partial r$ at the point (i, k) can be approximated as

$$\frac{\partial V_r}{\partial r} \approx \frac{\left(V_{r(i+1,k)}-V_{r(i-1,k)}\right)}{2\Delta r} \quad , \tag{2}$$

where Δr is the radial distance between two range gates, i is the index of the range gate and k the index of the elevation step. Similarly, $\partial V_\phi/\partial \phi$ at the point (i, k) can be approximated as

$$\frac{\partial V_\Phi}{\partial \Phi} \approx \frac{\left(V_{\Phi(i,k)}-V_{\Phi(i,k-1)}\right)}{\Delta \Phi} \quad . \tag{3}$$

Using Approximations 2 and 3, Eq. 1 can be modified to

$$V_{\Phi(i,k)} = V_{\Phi(i,k-1)} - \Delta\Phi V_{r(i,k)} - \frac{r\Delta\Phi}{2\Delta r}\left(V_{r(i+1,k)} - V_{r(i-1,k)}\right) \quad . \tag{4}$$

Equation 4 can be solved stepwise by starting at $\phi = 0°$, where $V_{\phi(i,k-1)} = 0$ and incrementing to $\phi = 90°$. Likewise, V_ϕ can be calculated from $\phi = 180°$ to $\phi = 90°$. However, in the case of divergence in y-direction, this leads to errors of $\partial V_r/\partial r$ resulting in errors of V_ϕ that propagate from one elevation increment to the next. This aliasing effect causes "rings" of high/low V_ϕ and large gradients of $\partial V_\phi/\partial\phi$. In order to mitigate the aliasing, a smoothing parameter S is introduced to average V_ϕ at the grid point (i, k-1) resulting in

$$V_{\Phi(i,k)} = \left[SV_{\Phi(i-1,k-1)} + (1-2S)V_{\Phi(i,k-1)} + SV_{\Phi(i+1,k-1)}\right] - \Delta\Phi V_{r(i,k)} - \frac{r\Delta\Phi}{2\Delta r}\left(V_{r(i+1,k)} - V_{r(i-1,k)}\right) \quad . \tag{5}$$

Tests with model and lidar fields show that best results are achieved with S in the range of 0.2 – 0.33 (see section 3). No significant improvements are achieved with a smoothing algorithm that includes the second-level of range gates (not shown). This smoothing algorithm is expected to reduce errors that arise due to the numerical approximations in Eqs. 2, 3 and due to the small-scale variability of the flow. However, the smoothing procedure does not remove errors arising from large-scale lateral flow divergence.

Without the along-beam smoothing, the method produces spurious structures of V_ϕ in some locations as mentioned above. This is understandable as errors due to lateral divergence in one range gate will propagate to higher elevations at constant Δr due to the iterative algorithm. However, divergence due to small-scale flow variability is usually compensated by convergence nearby. Thus, the spurious structures can be effectively mitigated through the smoothing

procedure, which is confirmed by the visual inspection of the results that shows realistic structures and no obvious rings after smoothing. The improvements through such an approach are further supported by the tests with output fields of the numerical model.

As a consequence, there is a difference of V_ϕ at $\phi = 90°$ for the calculation beginning with $\phi = 0°$ and $\phi = 180°$, respectively. Therefore, a correction is performed by assuming a constant error of ($V_{r(i+1,\ k)}$- $V_{r(i-1,\ k)}$) that is equal to the difference of the two V_ϕ calculations at $\phi = 90°$ divided by the number of elevation steps. Improvements of V_ϕ through such a correction are discussed in section 3.

After calculating V_ϕ, the vorticity field can be computed by using the definition of the spanwise vorticity component, η, in polar coordinates

$$\eta = \frac{1}{r}\frac{\partial}{\partial r}\left(rV_\Phi\right) - \frac{1}{r}\frac{\partial}{\partial \Phi}V_r \qquad (6)$$

For the vorticity calculation, $\partial V_\phi/\partial r$ and $\partial V_r/\partial \phi$ at the point (i, k) were approximated using centered finite differencing, similar to that in Eq. 2.

3. Evaluation of the velocity and vorticity calculations using model fields and T-REX observations

An example of T-REX lidar observations is shown in Fig. 2. A more detailed discussion of the rotor event on 16 April 2006 can be found in Doyle et al. (2009). The observations were taken during one of the strongest rotor events of T-REX and show strong downslope winds about 8-10 km upstream of the lidar. A region with weaker flow partly directed backwards towards the mountain range can be seen between the lidar and 5 km upstream of the lidar. Strong westerlies

are apparent above this region with weaker flow. A distinct vortex with a diameter of about 1 km that formed at the shear layer at about 3 km MSL is visible 2 km upstream of the lidar.

A vertical slice from the 3D high resolution numerical simulations using an eddy-resolving version of the COAMPS model was used to optimize the smoothing parameter S, to decide if the along-beam smoothing and the correction at V_ϕ = 90° should be applied and to estimate the uncertainty of the V_ϕ and vorticity calculation. The grid spacing of the simulations is 60 m in the horizontal and 50 m in the vertical (see Doyle et al. 2009). The baseline of the cross-section is the same as for the most common scan pattern during T-REX (roughly parallel to the main flow). There are obviously differences between the simulations (Fig. 2f) and the lidar observations (Fig. 2a), but the simulations appear to be a suitable test case as the strength and size of the vortices have a similar magnitude and structure. More details of the simulations, similarities and differences to T-REX observations are discussed in Doyle et al. (2009).

The model output fields were averaged to a polar grid that is similar to the lidar observations with a radial resolution of 105 m and 2.0054° for ϕ. In the vicinity of the lidar, where the resolution of the polar grid is higher than that the model grid, the angular tolerance for the averaging was increased by a factor of four for the first four range gates and by a factor of two for range gates 6-10. After averaging the model winds to a polar grid, V_r and V_ϕ were calculated (Figs. 2f and g). Additionally, V_ϕ was calculated from model V_r using the continuity equation, as discussed in section 2 (V_ϕ *-CONT*, Fig. 2g).

The spanwise vorticity was calculated from a vertical slice of the model test fields using three different methods: (1) Cartesian coordinates and then averaged to polar grid (not shown in Fig. 2); (2) polar coordinates using Eq. 6 with approximations described by Eqs. 7, 8 (Fig. 2i); (3) polar coordinates using V_ϕ calculated with the continuity equation (Fig. 2j, *VORT-CONT*). The

calculations for Figs. 2h were made using $S = 0.33$ and with a correction for differences of V_ϕ at $\phi = 90°$.

The standard deviation and mean of these fields are shown in Table 1. All values of Tables 1, 2 and 3 were only calculated for the domain where corrected V_ϕ-*CONT* is available (Fig. 2j) to make the values comparable. Table 2 shows the mean square differences of V_ϕ calculated using the continuity equation to the averaged model V_ϕ for a range of S from zero (no smoothing) to 0.33. The setting of $S = 0.33$ implies that the three range gates used for the averaging are nearly equally weighted. In addition, these fields are normalized with the mean square values of Table 1. Table 3 shows the vorticity differences in a similar manner as the V_ϕ differences are displayed in Table 2.

The V_ϕ and vorticity fields are calculated with simplified numerical approximations of the derivatives, which inevitable leads to numerical errors proportional to the grid increment. For this reason, the vorticity calculated in polar coordinates has smaller fluctuations than the vorticity calculated in Cartesian coordinates (Table 1). The calculation of V_ϕ using continuity and the smoothing parameter S lead to a further decrease of fluctuations that can be resolved by the method. However, small differences of the vorticity fields calculated in Cartesian coordinates and the ones in polar coordinates (not shown) indicate that these numerical errors are smaller than the ones resulting from divergence perpendicular to the lidar scan.

Figure 2h shows that the calculation of V_ϕ using continuity leads to reasonably accurate results in the region with fairly uniform flow (e.g., upstream -3 km and above 4 km MSL), but that lateral divergence can lead to errors of V_ϕ, for example in the turbulent region above the lidar, where the model fields show reversed flow in contrast to calculated V_ϕ. Despite these errors

of V_ϕ-*CONT*, the *VORT-CONT* in the same area is in reasonable agreement with the vorticity fields.

Overall, the error of V_ϕ-*CONT* is 6% of the total V_ϕ fluctuations for $S > 0.1$ with the correction for differences at $\phi = 90°$ and 7% for $S \geq 0.2$ without correction (Table 2). Both smoothing and the correction show a clear improvement of V_ϕ-*CONT*. According to the results, S should be in the range of 0.2-0.33 with lowest errors at $S = 0.33$. The total fluctuations of V_ϕ-*CONT* (Table 1) are realistic given the fact that the test field is highly turbulent.

The smoothing is assumed to reduce errors that primarily arise due to divergence perpendicular to the plane of the lidar scans associated with turbulent fluctuations. As a consequence, the optimal setting of S is expected to be dependent on the ratio of the dominant turbulence length scale and the resolution of the observations. The optimal *S*-parameter is defined as the value of S that leads to the smallest square difference of V_ϕ-*CONT* and *VORT-CONT* to model V_ϕ and vorticity, respectively. This dependency on S is demonstrated for the 3D simulation fields shown in Figure 3, where the optimal *S*-parameter is shown for different along-beam resolutions.

Further tests using a 2D simulation (Fig. 3) show that the smoothing parameter also improves the results in the absence of divergence perpendicular to the cross-section. Otherwise the optimal S parameter would be zero or close to zero for 2D model fields. This is interpreted as a reduction of numerical errors by the smoothing, which also explains why the optimal S parameter shows a clearly lower dependency on the along-beam resolution for the 2D fields. A direct comparison of the errors using 2D and 3D output fields is not possible as the flow field itself is significantly different in 2D and 3D simulations.

The error due to the vorticity calculation is less than 37% for $S \geq 0.2$ with the correction and less than 40% without correction. The smallest error of *VORT-CONT* is reached using

$S = 0.33$. With this setting, the error of the calculation is 34%, which implies that the vorticity derived using the continuity equation can explain 66% of the vorticity fluctuations. The positive effect of the correction actually does not appear to be that large for the vorticity field compared to the improvement of V_ϕ-*CONT*. This is understandable as only the gradients and not the absolute values of V_ϕ are important for the vorticity. The qualitative comparison of the results shown in Fig. 2 indicate reasonable agreement of the vorticity fields, the magnitude of the fluctuations of *VORT-CONT* is realistic (Table 1) and the maxima are of similar magnitude (~0.2 s^{-1}).

The application of the method to T-REX observations is shown in Figs. 2a-e. The qualitative interpretation of using different smoothing parameters for vorticity calculations with T-REX observations confirmed that $0.2 < S < 0.33$ is a reasonable choice for the parameter (not shown). As the calculation of V_ϕ needs a continuous field, five isolated missing values of V_r were interpolated from neighboring values for the calculation of V_ϕ and vorticity.

Despite differences of V_ϕ that arise due to the correction, the results for vorticity are very similar with and without the correction for differences at $\phi = 90°$ (Fig. 2). Due to the fact that observations at all elevation angles are needed to perform a correction, the coverage of corrected *VORT-CONT* is lower than that of the uncorrected field. In the field displayed in Fig. 2, this is clearly a limitation as the strongest vortex appearing at a height of 2 km AGL 1.7 km upstream of the lidar is not completely covered in the corrected field. The vorticity calculation has been tested with several of the lidar scans during T-REX and shows reasonable results in all cases. These tests confirm that the calculation leads to reasonable values for vorticity. The V_ϕ-*CONT* field is improved further with the inclusion of the correction factor.

4. Discussion

We have demonstrated that realistic vorticity fields can be derived from vertical slice lidar V_r-scans with a relatively simple and computationally inexpensive method that calculates V_ϕ solving the 2D continuity equation numerically. An along-beam smoothing of V_ϕ is essential to retain realistic results. A further correction for differences of V_ϕ at $\phi = 90°$ with a constant error term improves the fields of V_ϕ, but does not appear essential for the calculation of vorticity as only errors of the along-beam gradient of V_ϕ lead to vorticity errors, and not errors of the absolute V_ϕ.

Tests with an eddy-resolving model output from a 3D simulation reveal that the vorticity derived using the continuity equation can explain 66% of the vorticity fluctuations. In addition, the fluctuations of vorticity have a realistic magnitude and the calculation does not show a significant bias. The derived vorticity and model vorticity are qualitatively in good agreement. The V_ϕ field calculated from V_r using the continuity equation has an accuracy of 94%, but errors are larger in regions of strong turbulence.

The method is based on the assumption of 2D continuity, whereas the flow also has fluctuations in the third dimension perpendicular to the vertical slice. Thus, the main errors in the derived tangential velocity and vorticity result from small-scale flow variability and large-scale divergence in the third dimension. The first contributing factor should be mitigated through the along-beam smoothing. This is shown by tests with the velocity fields from the model simulations where the third velocity component is known. The errors due to large-scale flow divergence are attempted to be reduced through a correction based of the differences of V_ϕ at $\phi = 90°$ after calculating the tangential velocity incrementally from the surface on both sides of the lidar up to $\phi = 90°$. Without a large-scale flow divergence the calculations from both sides

should lead to the same tangential velocity at $\phi = 90°$. Thus, the V_ϕ-field was linearly relaxed to minimize the difference with this correction. Some of the remaining differences in the V_ϕ field indicate that the correction does not fully remove these errors. However, as illustrated by the model simulations, this large-scale flow divergence primarily affects the tangential velocity, and the derived vorticity is not substantially impacted. Instrumental noise associated with coherent Doppler lidars is estimated to be in a range of 0.1-0.3 m s^{-1} according to Grund et al. (2001) and Chai et al (2004), and thus comparably small to the velocity gradients of several m s^{-1} between neighboring range gates. Errors due to experimental noise can also be expected to be reduced by the along-beam smoothing as these errors are spatially uncorrelated.

In summary, the proposed method is useful to quantify the strength and size of vortices, such as those associated with atmospheric rotors, which pose a severe hazard to aviation. One limitation of the method is that only the spanwise vorticity component is derived. However, as there is no observing system that can observe the full 3D flow field within a time range of minutes, it is seen as a useful approach for topographic flow problems and other flows when the main wind component is along the plane of vertical slice lidar scans.

The along beam smoothing is performed through a weighted moving average of the neighboring range gates, whereby different weighting parameters for the average are investigated. The optimal smoothing parameter is expected to be dependent on eddy size, resolution of the observations and accuracy of the observing system. This smoothing may need to be adapted when the method is applied for different observing systems or if the vortices of interest are significantly different, but the general approach can be assumed to be valid for various applications where the strength of vorticity needs to be quantified by vertical cross-sections of line-of-sight observations from Doppler lidar or also Doppler radar instruments. In recent years, several airports around the world (e.g. Hong-Kong International Airport, Shun and Chan 2008) installed operational wind

lidar systems for aircraft safety and the presented method is also seen as a possibility to provide quantitative information on vortices and potential aviation hazards in real-time.

Acknowledgements

The efforts of the National Center for Atmospheric Research (NCAR) Field Project Support (FPS), and the T-REX staff are greatly appreciated. The primary sponsor of T-REX is the U.S. National Science Foundation (NSF), furthermore the DLR lidar observations were sponsored by funds from the Austrian Science Foundation (FWF) and internal funds of DLR. COAMPS® is a registered trademark of the Naval Research Laboratory (NRL). The third author acknowledges support through ONR PE 0601153N. The Doppler lidar operated by DLR was leased from Lockheed Martin Coherent Technologies and the technical support by Mark Vercauteren and Keith Barr is acknowledged. The assistance of Andreas Wieser (Forschungszentrum Karlsruhe) for DLR lidar observations, Matlab software from Ron Calhoun (ASU) and Christian Kühnlein (DLR) that provided the basis for the analysis of DLR lidar data, and help from Qingfang Jiang (NRL) with the formulation of the vorticity equation in polar coordinates are highly appreciated.

References

Chai, T., C.-L. Lin and R.K. Newsom, 2004: Retrieval of Microscale Flow Structures from High-Resolution Doppler Lidar Data Using an Adjoint Model. *J. Atmos. Sci.*, **61**, 1500-1520.

Doyle, J.D., and D.R. Durran, 2002. The Dynamics of Mountain-Wave Induced Rotors. *J. Atmos. Sci.*, **59**, 186-201.

Doyle, J.D., and D.R. Durran, 2007: Rotor and sub-rotor dynamics in the lee of three-dimensional terrain. *J. Atmos. Sci.*, **64**, 4202–4221.

Doyle, J.D., V. Grubišić, W,O.J. Brown, S.F.J. De Wekker, A. Dörnbrack, Q. Jiang, S.D. Mayor, M. Weissmann, 2009: Observations and numerical simulations of subrotor vortices during T-REX. *J. Atmos. Sci.,* **66**, 1229-1249.

Drechsel S., M. Chong, G. J. Mayr, M. Weissmann, R. Calhoun, and Andreas Dörnbrack, 2008: Three-dimensional wind retrieval: application of MUSCAT to dual Doppler lidar. *J. Atmos. Oceanic Technol.,* **26**, 635-646.

Grubišić, V., J.D. Doyle, J. Kuettner, S. Mobbs, R.B. Smith, C.D. Whiteman, R. Dirks, S. Czyzyk, S.A. Cohn, S. Vosper, M. Weissman, S. Haimov, S. De Wekker, L. Pan, and F.K. Chow, 2008: The Terrain-Induced Rotor Experiment: An overview of the field campaign and some highlights of special observations. *Bull. Amer. Meteor. Soc.,* **89**, 1513-1533.

Grund, C. J., R. M. Banta, J. L. George, J. N. Howell, M. J. Post, R. A. Richter, and A. M. Weickmann, 2001: High-resolution Doppler lidar for boundary layer and cloud research. *J. Atmos. Oceanic Technol.,* **18**, 376–393.

Hill, M., R. Calhoun, H. J. S. Fernando, A. Wieser, A. Dörnbrack, M. Weissmann, G. Mayr and R. Newsom, 2008: Coplanar Doppler Lidar Retrieval of Rotors from T-REX. *Submitted to J. Atmos. Sci.*

Holmboe, J., and H. Klieforth, 1957: Investigations of mountain lee waves and airflow over the Sierra Nevada. Final Rep., Contract AF19(604)-728, University of California ADNo. 133606, Dept. of Meteorology, University of California, Los Angeles, CA, 290 pp.

Kuettner, J., 1959: The rotor flow in the lee of mountains. *G.R.D. Res. Notes*, **6**, Air Force Cambridge Research Center, 20 pp.

Reitebuch, O., H. Volkert, C. Werner, A. Dabas, P. Delville, P. Drobinski, P. H. Flamant, and E. Richard, 2003: Determination of air flow across the Alpine ridge by a combination of airborne

Doppler lidar, routine radio-sounding, and numerical simulation. *Quart. J. Roy. Meteor. Soc.*, **129**, 715-728.

Shun C. M. and P. W. Chan, 2008: Applications of an Infrared Doppler Lidar in Detection of Wind Shear**.** *J. Atmos. Sci.*, **25**, 637-655.

FIGURE CAPTIONS

Figure 1: Schematic diagram of the Cartesian and cylindrical coordinate systems. The xz-plane and the rΦ-plane are chosen perpendicular to the valley axis, i.e. the x-axis is pointing towards an azimuth of 80° from north and the y-axis towards 350° from north. Lidar scans were performed mainly in the xz-plane and the rϕ-plane, which are roughly parallel to the main flow.

Figure 2: a) V_r measured by the DLR Doppler lidar during T-REX at 2134 UTC 16 April 2006. The scan is a vertical cross-section along a baseline from 260° (left) to 80° (right), which is roughly perpendicular to the valley axis. Observations were taken during an event with strong downslope winds to the lee of the Sierra Nevada. Cold colors indicate flow towards the lidar and warm colors flow away from the lidar. The topography is shown with a solid black line; b) V_ϕ calculated from (a) using the continuity equation, S = 0.33 and no correction for differences at $\phi = 90°$; c) same as (b) but calculated with correction for differences at $\phi = 90°$; d) vorticity using (a, b); e) vorticity using (a, c); f) V_r from model simulation along the same line as (a); g) V_ϕ from same model simulation as (f); h) V_ϕ calculated from (f) using the continuity equation, S = 0.33 and a correction for differences at $\phi = 90°$; i) vorticity calculated using (f, g); k) vorticity calculated using (f, h); all velocities are in m s^{-1}, all vorticity values in s^{-1}.

Figure 3: The S parameter leading to the lowest errors of the V_ϕ and vorticity calculation as a function of along-beam resolution in tests with 2D (solid lines) and 3D (dotted lines) model output fields.

FIGURES

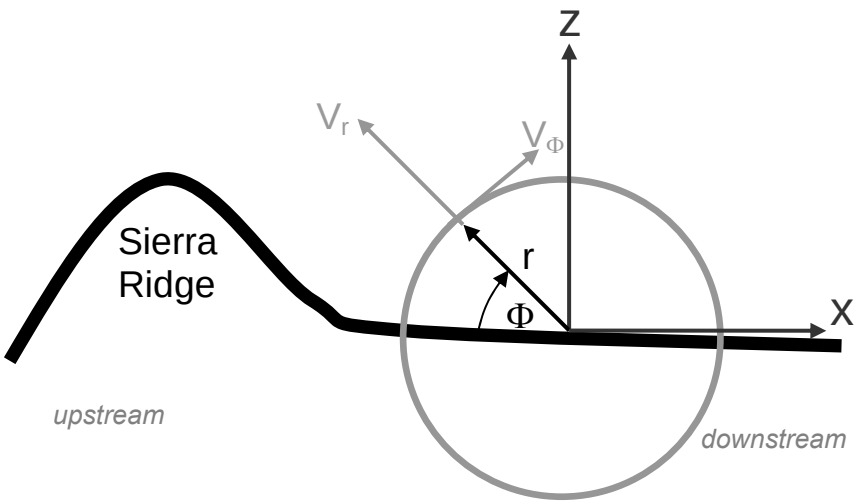

Figure 1: Schematic diagram of the Cartesian and cylindrical coordinate systems. The xz-plane and the rΦ-plane are chosen perpendicular to the valley axis, i.e. the x-axis is pointing towards an azimuth of 80° from north and the y-axis towards 350° from north. Lidar scans were performed mainly in the xz-plane and the rϕ-plane, which are roughly parallel to the main flow.

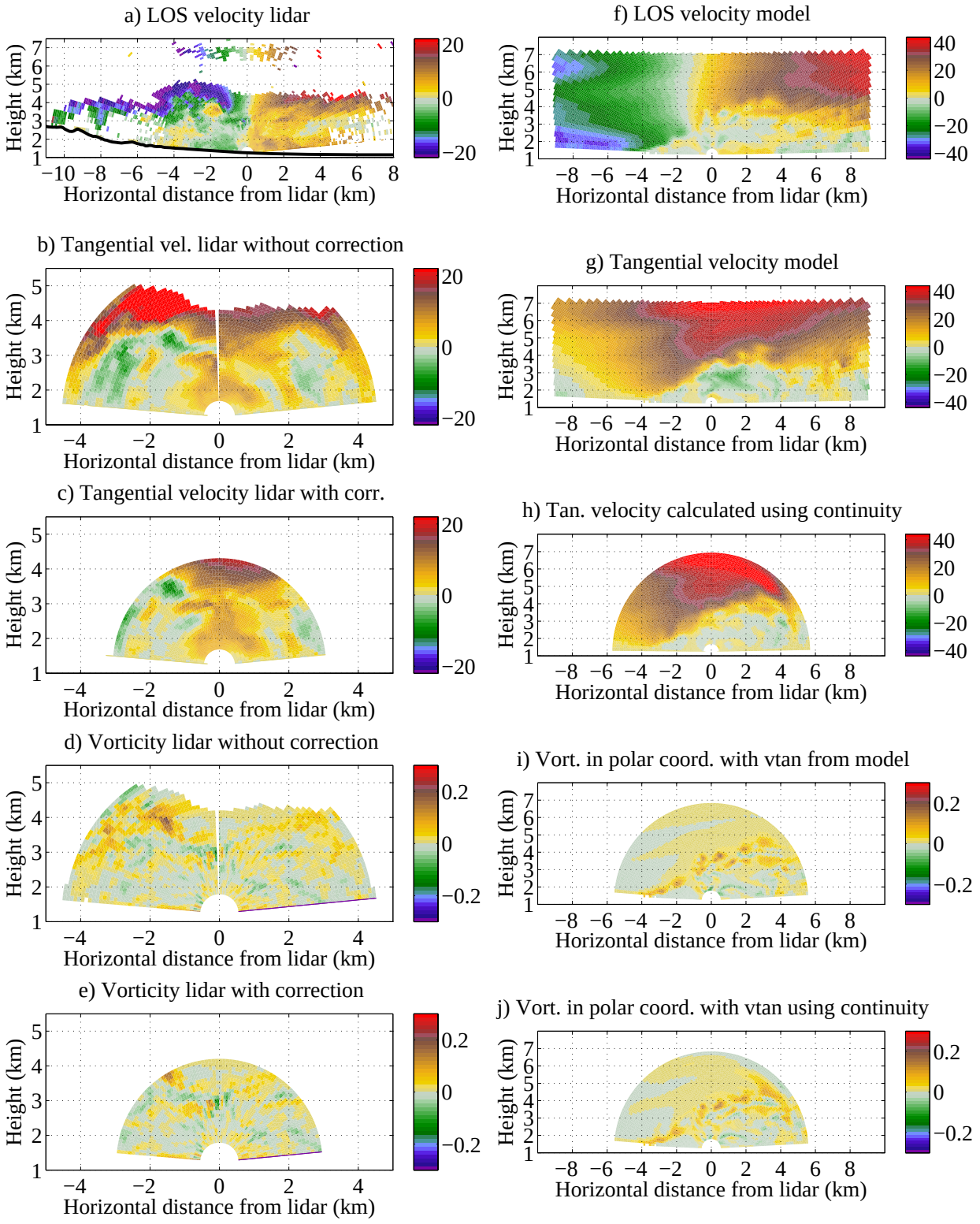

Figure 2: a) V_r measured by the DLR Doppler lidar during T-REX at 2134 UTC 16 April 2006. The scan is a vertical cross-section along a baseline from 260° (left) to 80° (right), which is roughly perpendicular to the valley axis. Observations were taken during an event with strong downslope winds to the lee of the Sierra Nevada. Cold colors indicate flow towards the lidar and

warm colors flow away from the lidar. The topography is shown with a solid black line; b) V_ϕ calculated from (a) using the continuity equation, S = 0.33 and no correction for differences at ϕ = 90°; c) same as (b) but calculated with correction for differences at ϕ = 90°; d) vorticity using (a, b); e) vorticity using (a, c); f) V_r from model simulation along the same line as (a); g) V_ϕ from same model simulation as (f); h) V_ϕ calculated from (f) using the continuity equation, S = 0.33 and a correction for differences at ϕ = 90°; i) vorticity calculated using (f, g); k) vorticity calculated using (f, h); all velocities are in m s^{-1}, all vorticity values in s^{-1}.

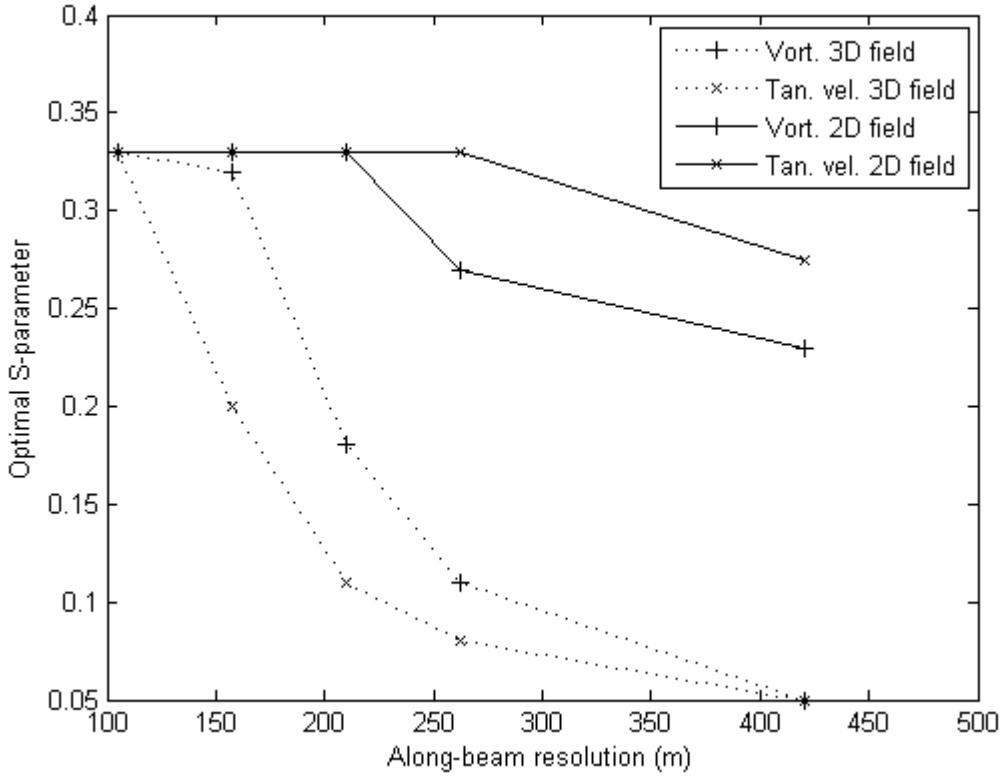

Figure 3: The S parameter leading to the lowest errors of the V_ϕ and vorticity calculation as a function of along-beam resolution in tests with 2D (solid lines) and 3D (dotted lines) model output fields.

TABLES

TABLE 1: Standard deviation and mean of vorticity and V_ϕ fields. The calculations were made with the correction for differences at $\phi = 90°$. The units of velocity are m s^{-1} and the ones of vorticity are s^{-1}.

	standard deviation	mean
vorticity from model interpolated	0.0298	0.0058
vorticity using model vtan	0.0278	0.0059
vorticity using continuity, S = 0.2	0.0270	0.0070
vorticity using continuity S = 0.33	0.0256	0.0070
V_ϕ from model	15.74	11.62
V_ϕ using continuity, S = 0.2	15.22	13.30
V_ϕ using continuity, S = 0.33	15.01	13.30

TABLE 2: Differences of V_ϕ calculated from model V_r using the continuity equation with a correction for differences at $\phi = 90°$ and model V_ϕ. The values are normalized with values shown in table 1.

smoothing parameter S	0.00	0.10	0.20	0.30	0.33
relative mean square diff (V_ϕ corr.)	0.08	0.06	0.06	0.06	0.06
relative mean square diff (V_ϕ no corr.)	0.10	0.08	0.07	0.07	0.07

TABLE 3: Differences of vorticity calculated using the continuity equation with a correction for differences at $\phi = 90°$ and vorticity calculated from model velocities averaged to polar grid.

smoothing parameter S	0.00	0.10	0.20	0.30	0.33
mean square diff(vort_corr) in 10^{-4} m^2 s^{-2}	5.82	3.60	3.01	2.78	2.73
relative mean square diff (corr.)	0.72	0.45	0.37	0.34	0.34
mean square diff(vort_nocorr) in 10^{-4} m^2 s^{-2}	7.32	4.00	3.22	2.90	2.85
relative mean square diff (no corr.)	0.91	0.49	0.40	0.36	0.35